9-2016

Monitoring of Tissue Optical Properties During Thermal Coagulation of *ex vivo* Tissues

Vivek K. Nagarajan
The University of Akron

Bing Yu
Marquette University, bing.yu@marquette.edu

Lasers in Surgery and Medicine, Vol. 48, No. 7 (September 2016): 686-694. DOI.

Monitoring of Tissue Optical Properties During Thermal Coagulation of Ex Vivo Tissues

Vivek Krishna Nagarajan
University of Akron
Bing Yu
University of Akron, Marquette University

Abstract

Background and Objective

Real-time monitoring of tissue status during thermal ablation of tumors is critical to ensure complete destruction of tumor mass, while avoiding tissue charring and excessive damage to normal tissues. Currently, magnetic resonance thermometry (MRT), along with magnetic resonance imaging (MRI), is the most commonly used technique for monitoring and assessing thermal ablation process in soft tissues. MRT/MRI is very expensive, bulky, and often subject to motion artifacts. On the other hand, light propagation within tissue is sensitive to changes in tissue microstructure and physiology which could be used to directly quantify the extent of tissue damage. Furthermore, optical monitoring can be a portable, and cost-effective alternative for monitoring a thermal ablation process. The main objective

of this study, is to establish a correlation between changes in tissue optical properties and the status of tissue coagulation/damage during heating of *ex vivo* tissues.

Materials and Methods

A portable diffuse reflectance spectroscopy system and a side-firing fiber-optic probe were developed to study the absorption ($\mu_s'(\lambda)$) and reduced scattering coefficients ($\mu_s'(\lambda)$) of native and coagulated *ex vivo* porcine, and chicken breast tissues. In the first experiment, both porcine and chicken breast tissues were heated at discrete temperature points between 24 and 140°C for 2 minutes. Diffuse reflectance spectra (430–630 nm) of native and coagulated tissues were recorded prior to, and post heating. In a second experiment, porcine tissue samples were heated at 70°C and diffuse reflectance spectra were recorded continuously during heating. The $\mu_a(\lambda)$ and $\mu_s'(\lambda)$ of the tissues were extracted from the measured diffuse reflectance spectra using an inverse Monte-Carlo model of diffuse reflectance. Tissue heating was stopped when the wavelength-averaged scattering plateaued.

Results

The wavelength-averaged optical properties, $< \mu_s'(\lambda) >$ and $< \mu_a(\lambda) >$, for native porcine tissues (*n* = 66) at room temperature, were 5.4 ± 0.3 cm^{-1} and 0.780 ± 0.008 cm^{-1} (SD), respectively. The $< \mu_s'(\lambda) >$ and $< \mu_a(\lambda) >$ for native chicken breast tissues ($n = 66$) at room temperature, were 2.69 ± 0.08 cm^{-1} and 0.29 ± 0.01 cm^{-1} (SD), respectively. In the first experiment, the $< \mu_s'(\lambda) >$ of coagulated porcine and chicken breast tissue rose to 56.4 ± 3.6 cm^{-1} at 68.7 ± 1.7°C (SD), and 52.8 ± 1 cm^{-1} at 57.1 ± 1.5°C (SD), respectively. Correspondingly, the $< \mu_a(\lambda) >$ of coagulated porcine (140.6°C), and chicken breast tissues (130°C) were 0.75 ± 0.05 cm^{-1} and 0.263 ± 0.004 cm^{-1} (SD). For both tissues, charring was observed at temperatures above 80°C. During continuous monitoring of porcine tissue (with connective tissues) heating, the $< \mu_s'(\lambda) >$ started to rise rapidly from 13.7 ± 1.5 minutes and plateaued at 19 ± 2.5 (SD) minutes. The $< \mu_s'(\lambda) >$ plateaued at 11.7 ± 3 (SD) minutes for porcine tissue devoid of connective tissue between probe and tissue surface. No charring was observed during continuous monitoring of thermal ablation process.

Conclusion

The changes in optical absorption and scattering properties can be continuously quantified, which could be used as a diagnostic biomarker for assessing tissue coagulation/damage during thermal ablation.

INTRODUCTION

The sensitivity of tumor cells to heat was first observed more than a century ago [1]. The thermosensitivity of tumor cells as compared to their associated normal cells has enabled the wide use of hyperthermia in cancer therapy. The narrative for hyperthermia in cancer therapy has been well documented by Cavaliere et al. [2]. Today, thermal ablation of solid tumors is being used ubiquitously for treating inoperable tumors [3-7]. The main objective of a thermal ablation procedure is to completely coagulate the malignant tumor cells with minimal, or no thermal damage to the surrounding normal cells.

To ensure complete tumor ablation, current practices ablate a small margin of surrounding normal tissues, in addition to the target tumor tissue. However, such practices are not tissue sparing and may not be feasible when tumors are near critical structures such as major nerves, blood vessels, or organs [8-11]. Excessive thermal ablation of tissue (normal or tumor) leads to undesirable effects such as tissue charring which complicates ablative procedures [12-15]. Therefore, continuous monitoring of a thermal ablation process is vital for achieving complete and optimal tumor ablation. Monitoring of thermal ablation procedures usually entails image-guidance for locating the tumor and placement of probes/electrodes, as well as assessment of the thermal damage to the target tissue. The assessment of thermal tissue damage is usually done using the Arrhenius damage integral Equation 1 [16].

$$\Omega = \ln\left(\frac{c(0)}{c(t)}\right) = \int_0^t Ae\,\frac{(-E_a)}{(RT)}\,dt \quad (1)$$

Where Ω is the degree of damage, A is the Arrhenius exponential factor, E_a is the activation energy, R is the gas constant, and T is the temperature in Kelvin, $c(0)$ is the concentration of the native molecules, and $c(t)$ is the concentration of denatured molecules. Tissue coagulation is assumed to be a unimolecular reaction which facilitates in the estimation of Ω. E_a and A are experimentally determined. Thus, only temperature and duration of heating are required to determine Ω. MRI [17] along with magnetic resonance thermometry (MRT) [18] is the most commonly used technique for providing image-guidance, and temperature information during ablation procedures. They have been used in conjunction with radiofrequency ablation [19-21], microwave ablation, high intensity focused ultrasound [22], or laser interstitial thermal therapy [23] for providing image guidance and temperature estimation.

Temperature-based estimation of tissue damage is an indirect method for assessing the degree of damage. During a coagulation process, tissues undergo both microscopic and macroscopic changes in their structures, and physiological functions. Monitoring such changes would be a more direct approach to assess the extent of thermal damage. Quantitative diffuse reflectance spectroscopy (DRS) is a non-destructive method that is sensitive to tissue absorption and scattering, and thus, can be used to quantify the tissue morphological, and physiological properties *in vivo* [24-26]. The light scattering is sensitive to changes in tissue microstructure, while light absorption is dependent on the distribution of chromophores within a tissue. Therefore, continuous monitoring of changes in tissue absorption, and scattering properties would help in assessing the tissue status during an ablation procedure to achieve the desired treatment endpoints.

In the past decade many groups have reported differences in the tissue absorption, and scattering coefficients of native and coagulated tissues [27-34]. Several studies reported an increase in fluorescence in coagulated tissue [35-39]. It has been demonstrated that spectra ratios could also be used as a tool to assess tissue coagulation [36-38, 40-44]. In all these studies, the common findings for coagulated tissues include decreased light penetration, increased light scattering, and/or an increase in tissue fluorescence. However, techniques used in [27-34, 45] for extracting tissue absorption and scattering requires tissue sectioning, and/or an integrating sphere which are not applicable *in vivo*, spectral ratios are sensitive to instrument drifts, and fluorescence-based methods require complex and expensive

hardware. A robust and low-cost system for determining tissue optical properties ($\mu_a(\lambda)$, and $\mu_s'(\lambda)$) during an ablation process is yet to be realized in a clinical setting. In this paper, we report the development of a portable DRS system and a side-firing fiber-optic probe for monitoring the real-time changes in tissue optical properties in the visible wavelength range during thermal ablation, and experimental results from *ex vivo* porcine and chicken breast tissues during heating. The resulting data substantiates the changes in the tissue absorption, and scattering during heating which paves the way for an online ablation monitoring system using quantitative DRS.

MATERIALS AND METHODS

DRS Instrument

The DRS system consists of a home-made side-firing fiber-optic probe, a customized visible spectrometer (Avantes BV, The Netherland) with a white light-emitting-diode (LED) as the light source, and a laptop loaded with custom software, shown in Figure **1**. The fiber-optic probe consists of two side-firing fibers (200 µm), spaced apart by 1.53 mm, and mounted onto a V-groove in a Delrin plate ($4 \times 8 \times 5$ mm) [46]. One of the fibers was connected to the white LED to illuminate the target, and the other was used as the detection fiber which was connected to the spectrometer. The laptop computer with a custom LabVIEW program and embedded Matlab scripts were used for instrument control, and data acquisition and analysis.

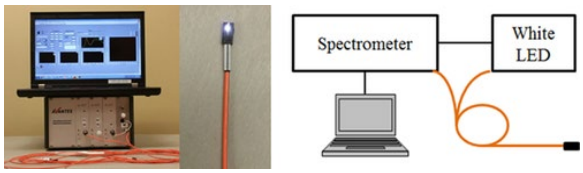

Figure 1. **Left**: Image of the visible DRS system and fiber-optic probe. **Right**: Schematic of the DRS system with the side-firing fiber-optic probe.

Tissue Phantom Experiment

A tissue phantom experiment was used to evaluate the performance of the fiber-optic probe for measuring tissue optical properties. The tissue-mimicking phantoms consisted of a mixture of human Hemoglobin (Hb) powder (H0267, Sigma–Aldrich Co. LLC, St Louis, MO), as the absorber, and 1-µm Polystyrene beads (07310-15, Polysciences, Inc., Warrington, PA), as the tissue scatterer in water. Twenty-one phantoms covering a hemoglobin concentration of $4.41 – 48$ µM were created by fixing the number of scatterers, and titrating the absorbers. Diffuse reflectance spectrum ($430 – 630$ nm) for each of the 21 phantoms were collected using the fiber-optic probe and the DRS instrument. The absorption coefficient $\mu_a(\lambda)$ of stock Hemoglobin solution was independently determined with a spectrophotometer (Lambda 35, PerkinElmer, Inc., Waltham, MA). The wavelength-averaged absorption coefficient $< \mu_a(\lambda) >$ of the 21 phantoms ranged from 0.3 to 3.28 cm^{-1}. The reduced scattering $\mu_s'(\lambda)$ of the phantoms was calculated using the Mie theory for known size, density, and refractive index of scatterers. The wavelength-averaged reduced scattering coefficient, $< \mu_s'(\lambda) >$, decreased from 38.3 to 18.5 cm^{-1} due to absorber titration, representing the typical scattering properties of coagulated porcine muscle, and chicken breast tissues.

Ex Vivo Experiments

Porcine loin muscle and chicken breast muscle were purchased fresh from a local meat shop and stored at 4°C to minimize water evaporation, and mechanical damages. All tissue samples were used within 1–2 days of purchase. Before each measurement, tissue samples were allowed to warm up at room temperature (22°C) for 7 minutes. For both chicken and porcine tissues, 66 samples $(22 \times 21 \times (12\text{–}16)\,\mathrm{mm})$, from at least five biological replicates, were cut, and randomized to account for inter-individual differences. The baseline DRS measurements (430–630 nm) were taken from each native sample tissue. Two experiments have been performed with the *ex vivo* porcine and chicken samples.

Ex vivo experiment 1

The hotplate surface was set to the testing temperature which was confirmed with a J-type surface thermocouple. The tissue samples were heated on the hotplate for 2 minutes, as shown in Figure **2**a. The temperature of the tissue was monitored at a point 3 mm away from the heated surface using a needle-based J-type thermocouple to avoid disturbing the light path within the tissue. Placing the thermocouple close to the mean photon travel depth can alter the propagation of photons within the target tissue which would induce errors in the extracted $\mu_s'(\lambda)$, and $\mu_a(\lambda)$. Patterson et al. [47] reported a relationship for estimating mean photon travel depth within the tissue using source-detector separation under steady-state condition. The mean photon travel depth for baseline tissue was estimated to be 1 mm (porcine) and 1.44 mm (chicken). The mean photon depth for coagulated tissue reduced to 0.580 mm (porcine) and 0.770 mm (chicken). So, a distance of 3 mm, little more than twice the mean photon travel depth in chicken tissue, was used for placing the thermocouple. The temperatures measured by both the thermocouples (hotplate and within tissue) were averaged to denote the tissue temperature (T). After which, samples were removed from the hotplate and allowed to cool in room temperature (22°C) for 7 minutes prior to measurement. A set of 10 diffuse reflectance measurements were recorded from the same site for each tissue sample. For each tissue sample, T, duration (t), tissue images, and diffuse reflectance spectra were recorded for analysis.

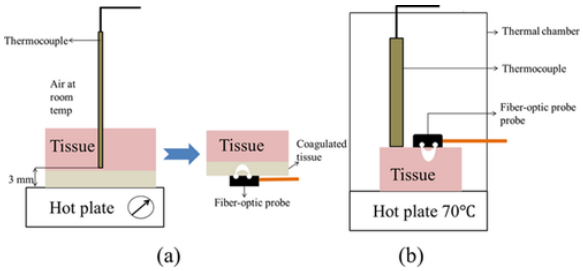

Figure 2 Experimental setups (**a**) Tissue is heated for 2 minutes at different temperatures and cooled at room temperature for 7 minutes before measurement. (**b**) Real-time changes in tissue optical properties are measured continuously during heating.

Ex vivo experiment 2

In the second experiment, porcine (with and without connective tissue between probe, and tissue surface) tissue samples were used to monitor the changes in $< \mu_s'(\lambda) >$, and $< \mu_a(\lambda) >$ during heating. The fiber-optic probe was placed onto the surface of the tissue, which in turn was mounted onto the hotplate (pre-heated to 70°C), as shown in Figure **2**b. The DRS measurements and time were

continuously recorded during heating until $< \mu_s'(\lambda) >$ plateaued. The tissue samples were covered in a metal enclosure through the experiment to achieve a more uniform heating.

Data Analysis

The diffuse reflectance spectra measured from the 21 phantoms were analyzed using a Monte-Carlo (MC) inverse model of reflectance to extract the phantom $\mu_a(\lambda)$, and $\mu_s'(\lambda)$. A detailed description of the MC model can be found in Ref. [48]. In brief, the model iteratively fits the modeled reflectance spectrum that is calculated with guessed input parameters ($\mu_a(\lambda)$, and $\mu_s'(\lambda)$) to the measured reflectance spectrum. Upon convergence, the $\mu_a(\lambda)$ and $\mu_s'(\lambda)$ are extracted. Each of the 21 phantoms was used as a reference to invert all phantoms. The reference phantom that introduced the least overall error was chosen as the reference to invert the diffuse reflectance spectra obtained in the tissue experiments. The extracted $\mu_a(\lambda)$ and $\mu_s'(\lambda)$ are averaged over the wavelength range (430–630 nm). The variations reported in all measurements are standard deviations of the mean (SD).

Student's *t*-test (Significance level $\alpha = 0.05$) is used for comparing the differences in wavelength-averaged optical properties, $< \mu_s'(\lambda) >$ and $< \mu_a(\lambda) >$, of native, and coagulated tissues in both experiments. The $< \mu_s'(\lambda) >$ and $< \mu_a(\lambda) >$ at coagulation temperature for both tissues were also compared. In the second experiment, T, $< \mu_s'(\lambda) >$ and $< \mu_a(\lambda) >$ at the start of plateau were compared with those obtained in the first experiment. The extracted baseline $< \mu_s'(\lambda) >$ and $< \mu_a(\lambda) >$ in first, and second experiment were also compared. In addition, Arrhenius parameters (E_a and A) of sarcoplasmic proteins and collagen, myosin, and actin in porcine sirloin muscle, reported by Kajitani et al. [49], and duration (*t*) were used to calculate Ω and the degree of denaturation (F_d) for porcine tissue, Equation 2. The F_d is derived from Equation 1 by a simple rearrangement of terms. An $F_\mathrm{d} = 1$ signifies complete denaturation, whereas, $F_\mathrm{d} = 0$ indicates no thermal denaturation, or native tissue. Due to unavailability of E_a and A for chicken tissue, the F_d could not be calculated.

$$F_\mathrm{d} = 1 - e^{-\Omega} = \frac{c(t) - c(0)}{c(0)} \quad (2)$$

RESULTS

Phantom Experiment

The $< \mu_a(\lambda) >$ and $< \mu_s'(\lambda) >$, from each phantom are compared with the expected values, and the results are plotted in Figure **3**. The overall errors for extracting $< \mu_s'(\lambda) >$ and $< \mu_a(\lambda) >$ of the tissue-mimicking phantoms were 10.2% and 6.7%, respectively. A second phantom experiment, Figure **3**, was conducted to cover the range of $< \mu_s'(\lambda) >$ for coagulated porcine, and chicken tissue. Here, we observed an overall error of 16.3% in $< \mu_s'(\lambda) >$ ($40.7 – 56.9$ cm^{-1}), and 27.5% in $< \mu_a(\lambda) >$ ($0.46 – 2.28$ cm^{-1}).

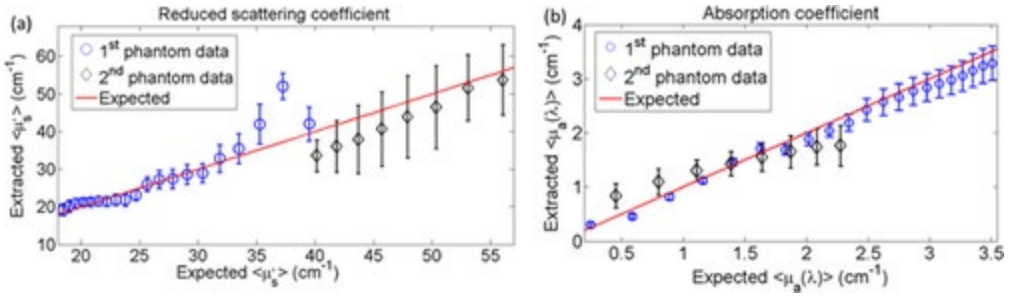

Figure 3 The extracted and expected (**a**) $< \mu_s'(\lambda) >$ and (**b**) $< \mu_a(\lambda) >$ of the tissue-mimicking phantoms.

Ex Vivo Experiment 1

The diffuse reflectance spectra from each sample tissue were recorded from both native, and coagulated tissue. The measured $< \mu_s'(\lambda) >$ and $< \mu_a(\lambda) >$ for the porcine native tissue ($n = 66$) were 5.4 ± 0.3 cm^{-1}, and 0.780 ± 0.008 cm^{-1}, respectively. There are very few studies, that have reported porcine optical properties for the range ($430-630$ nm), which limits us from comparing our extracted porcine muscle optical properties with other studies. Alali et al. [50] reported $\mu_s'(\lambda) = 4 \pm 0.07$ cm^{-1} and $\mu_a(\lambda) = 0.37 \pm 0.04$ cm^{-1} at 635 nm for porcine muscles which were significantly different from the $< \mu_s'(\lambda) >$ (4.9 ± 0.7 cm^{-1}, $P = 0.002$), and $< \mu_a(\lambda) >$ (0.022 ± 0.004 cm^{-1}, $P < 0.0001$) at 630 nm, measured in this study. The measured $< \mu_s'(\lambda) >$ and $< \mu_a(\lambda) >$ for chicken breast native tissues ($n = 66$) are 2.69 ± 0.08 cm^{-1}, and 0.29 ± 0.01 cm^{-1}, respectively. The $\mu_s'(\lambda)$ and $\mu_a(\lambda)$ for chicken muscle at 633 nm can vary between ($3.3-8$ cm^{-1}) and ($0.12-0.17$ cm^{-1}), respectively [51]. Kienle et al. [52] reported $\mu_s'(\lambda) = 4.2 \pm 0.5$ cm^{-1} and $\mu_a(\lambda) = 0.038 \pm 0.008$ cm^{-1} at 633 nm for chicken breast tissues which were significantly different from the $< \mu_s'(\lambda) >$ (3.34 ± 0.3 cm^{-1}, $P < 0.0001$), and $< \mu_a(\lambda) >$ (0.011 ± 0.003 cm^{-1}, $P < 0.0001$) at 630 nm, measured in this study. The $< \mu_s'(\lambda) >$ and $< \mu_a(\lambda) >$ of the porcine tissues measured after heating at various temperatures are shown in Figure **4**a and b. For visual comparison, images of coagulated porcine tissue samples at selected temperatures are also shown in Figure **4**c. The $< \mu_s'(\lambda) >$ in Figure **6**a starts to rise at the complete denaturation ($F_d = 1$) of myosin, and plateaus at the complete denaturation of actin. This shows that $< \mu_s'(\lambda) >$ is strongly affected by tissue denaturation. On the other hand, the $< \mu_a(\lambda) >$, Figure **6**b, showed no clear change with tissue denaturation. However, the $< \mu_a(\lambda) >$ increases above 100°C. The $< \mu_s'(\lambda) >$ and $< \mu_a(\lambda) >$ of the chicken breast tissues measured at the end of heating are shown in Figure **5**a and b. For visual comparison, images of coagulated chicken breast tissue samples at selected temperatures are also shown in Figure **5**c.

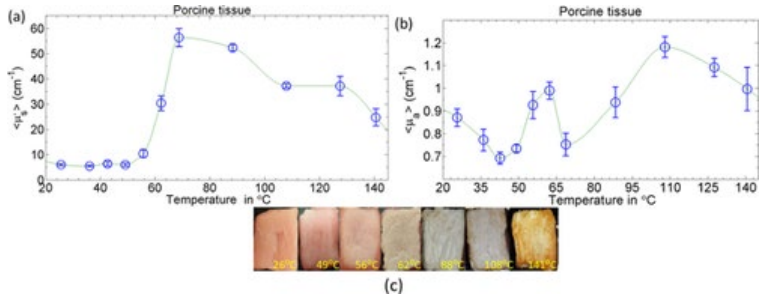

Figure 4 Porcine muscles: (**a**) $< \mu_s'(\lambda) >$, (**b**) $< \mu_a(\lambda) >$. (**c**) Images of porcine muscle tissue captured after heating at different temperatures.

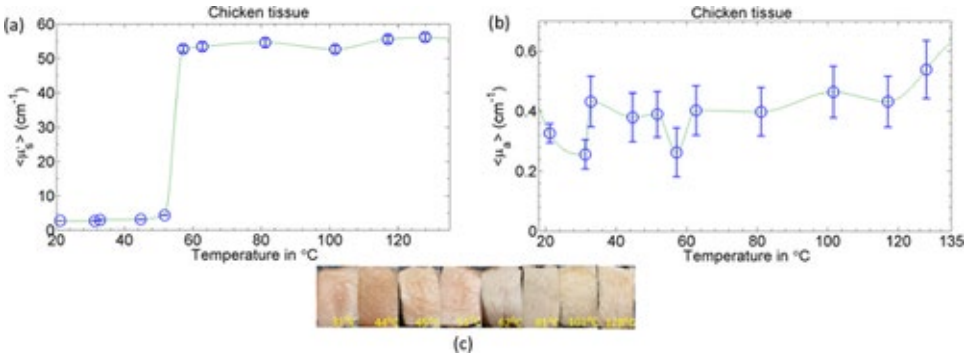

Figure 5 Chicken breast tissues: (**a**) $< \mu_s'(\lambda) >$, (**b**) $< \mu_a(\lambda) >$. (**c**) Images of chicken breast tissue captured after heating at different temperatures.

The reduced scattering coefficient increased from 5.4 ± 0.3 cm^{-1} to 30.4 ± 2.9 cm^{-1} ($P < 0.0001$) between 49–67°C (porcine), and 2.69 ± 0.08 cm^{-1} to 53.4 ± 0.35 cm^{-1} ($P < 0.0001$) between 45 and 63°C (chicken breast). On the contrary, the absorption coefficient increased from 0.780 ± 0.008 cm^{-1} to 0.99 ± 0.25 cm^{-1} ($P < 0.0001$) for porcine tissues heated to 140.6°C, and from 0.29 ± 0.01 cm^{-1} to 0.54 ± 0.01 cm^{-1} ($P < 0.0001$) for chicken tissues heated to 130°C. The $< \mu_s'(\lambda) >$ at coagulation temperatures for porcine (56.4 ± 3.6 cm^{-1}) and chicken (52.8 ± 1 cm^{-1}) were significantly different ($P = 0.04$). Also, tissue coagulation was visually observable from 49°C (porcine), Figure **4**c, and 45°C (chicken), Figure **5**c on the heated tissue surface.

Ex Vivo Experiment 2

In the second *ex vivo* experiment, real-time values of $< \mu_a(\lambda) >$ and $< \mu_s'(\lambda) >$ of porcine tissues (with ($n = 6$) and without ($n = 6$) connective tissue between probe, and tissue surface) were recorded continuously during heating using the setup in Figure **2**b. For porcine tissue with connective tissues (Fig. **7**a and b), a sharp dip in $< \mu_s'(\lambda) >$ was observed at 12.2 minutes, 45 seconds later the $< \mu_s'(\lambda) >$ began to rise, and eventually reached a plateau. Overall, the $< \mu_s'(\lambda) >$ dipped at 12.4 ± 1.5 minutes ($n = 6$), and began to rise systematically from 13.7 ± 1.5 minutes to plateau at 19 ± 2.5 minutes with a measured temperature of 63.6 ± 0.7°C. The $< \mu_s'(\lambda) >$ at the dip of the samples were not significantly different from the baseline measurements of porcine muscle measured in the first experiment ($P < 0.3603$, $n = 6$). On the other hand, a sharp increase in $< \mu_a(\lambda) >$ was observed at the same time as the dip in $< \mu_s'(\lambda) >$, after which, $< \mu_a(\lambda) >$ continued to rise until 13.7 ± 1.5 minutes, and dropped sharply. The $< \mu_a(\lambda) >$ at the jump was significantly different from the baseline optical properties of porcine muscle measured in the first experiment ($P < 0.001$, $n = 6$). The extracted $< \mu_a(\lambda) >$ continued to decrease until 19 ± 2.5 minutes at 63.6 ± 0.7°C. For porcine tissue without connective tissues (Fig. **7**c and d), a sharp jump in $< \mu_s'(\lambda) >$ was observed at 11.7 ± 3 minutes. The $< \mu_a(\lambda) >$ increased gradually from baseline by $44 \pm 30\%$ and dropped sharply at 11.7 ± 3 minutes.

DISCUSSION

Real-time monitoring of tissue status during thermal ablation is critical for achieving an optimal tumor therapy. Excessive thermal ablation of tissue (normal or tumor) leads to undesirable effects such as tissue charring, which complicates the ablative procedures [12-15]. On the other hand, insufficient heat will lead to partial ablation, consequently increased risk of local recurrences of tumor [12]. In this study, a fiber-optic DRS system was developed to collect diffuse reflectance spectra in the visible wavelength

range from *ex vivo* porcine and chicken breast tissues prior to, post, and during coagulation. The $< \mu_a(\lambda) >$ and $< \mu_s'(\lambda) >$ of tissue samples were extracted from the measured spectra using an inverse Monte-Carlo model of reflectance. The system showed a decent accuracy for quantifying $< \mu_a(\lambda) >$ and $< \mu_s'(\lambda) >$ of liquid phantoms, representative of native, and coagulated porcine and chicken breast tissues.

In the first tissue experiment, the $< \mu_s'(\lambda) >$ of porcine tissues increased from baseline to 30.4 ± 2.9 cm^{-1} between 49 and 63°C, and began to decrease at higher temperatures as shown in Figure **4**a. The decrease in $< \mu_s'(\lambda) >$ in Figure **4**a could have been partly due to the tissue carbonization. Correspondingly, a 28.5% increase from the baseline in $< \mu_a(\lambda) >$ of porcine tissue samples was observed at 140.6°C (the highest temperature studied), likely due to tissue carbonization. However, tissue shrinkage during thermal denaturation is also known to increase the absorption coefficient [53]. The carbon deposits which resulted in a brown-black coloration of the coagulated pork tissue sample can be visually seen in Figure **4**c. For the chicken breast tissue samples, $< \mu_s'(\lambda) >$ increased from baseline to 52.8 ± 1 cm^{-1} between 51 and 58°C, and plateaued, as shown in Figure **5**a. No decrease in $< \mu_s'(\lambda) >$ was observed at higher temperature. Minimal tissue carbonization was observed at temperatures above 60°C. A 52.9% increase in $< \mu_a(\lambda) >$, from baseline, was observed at 130°C (the highest temperature studied). The $< \mu_s'(\lambda) >$ of coagulated porcine (56.4 ± 3.6 cm^{-1}) at 68.7 ± 0.7°C and chicken breast tissues (52.8 ± 1 cm^{-1}) at 57.1 ± 1.5°C, were significantly different ($P = 0.04$). Similar results have been reported by Thomsen et al. [54] who observed a twofold increase in $< \mu_a(\lambda) >$ and a fivefold increase in $< \mu_s'(\lambda) >$ (at 594 and 634 nm) in rat myocardium between 45–65°C and 60–70°C, respectively. The Thomsen study also observed plateauing of $< \mu_s'(\lambda) >$ at 65 (594 nm) and 70°C (634 nm), respectively.

In the second tissue experiment, real-time changes in $< \mu_s'(\lambda) >$ and $< \mu_a(\lambda) >$ of porcine muscles were recorded during heating (Fig. **7**). For porcine tissue without connective tissues, Figure **7**c and d, a sharp jump in $< \mu_s'(\lambda) >$ was observed at 11.7 ± 3 minutes. The $< \mu_a(\lambda) >$ increased gradually by $44 \pm 30\%$ and dipped sharply at 11.7 ± 3 minutes. The corresponding temperature was 48.9 ± 1.2°C. The sharp changes in $< \mu_s'(\lambda) >$ and $< \mu_a(\lambda) >$ in Figure **7**c and d may be due to the rapid transformation of tissue microstructure due to thermocoagulation. Rapid denaturation of some major muscle constituents such as sarcoplasmic proteins and collagen, myosin, and actin between 65 and 70°C can be observed from Figure **6**. Unlike the $< \mu_s'(\lambda) >$ of porcine tissue without connective tissue, Figure **7**c, the measured baseline $< \mu_s'(\lambda) >$ of porcine tissues with connective tissue, Figure **7**a, was several times higher than those measured in the first tissue experiment (Fig. **4**a). The higher baseline $< \mu_s'(\lambda) >$ in Figure **7**a could have been due to the presence of connective tissue covering the surface of the porcine muscle tissues. Melting of the connective tissue exposes the muscle tissue to the fiber-optic probe, and improving the probe contact with the underlying tissue, thus, resulting in a sharp change in the measured optical properties. The light scattering within the tissue is a result of the refractive index mismatch between scattering centers (cell nuclei, collagen fiber, mitochondria, subcellular organelles) and surrounding media (extra or intracellular fluid) within the tissue. A lower mismatch in refractive index will result in decreased light scattering [53]. This could have resulted in the decrease of baseline $< \mu_s'(\lambda) >$ (Fig. **7**a) from 29 ± 3.9 cm^{-1} (baseline) to 4 ± 0.1 cm^{-1} (dip). Interestingly, the $< \mu_s'(\lambda) >$ (Fig. **7**a) at the dip of the samples in the second experiment was not significantly different from the baseline of porcine muscle measured in the first experiment ($P <$

$0.3603,\ n\ =\ 6$), which could have been due to the improved probe-tissue contact. From the dip, the $<\mu_s'(\lambda)>$ follows a similar trend to Figure **7**c, rising to a plateau. The $<\mu_a(\lambda)>$ (Fig. **7**b) changed from $0.4\ \pm\ 0.1$ cm^{-1} at the baseline to $0.6\ \pm\ 0.1$ cm^{-1}at the dip. However, the $<\mu_a(\lambda)>$ in (Fig. **7**b), at the jump, was significantly different from the baseline optical properties of porcine muscle measured in the first experiment ($P\ <\ 0.001,\ n\ =\ 6$).

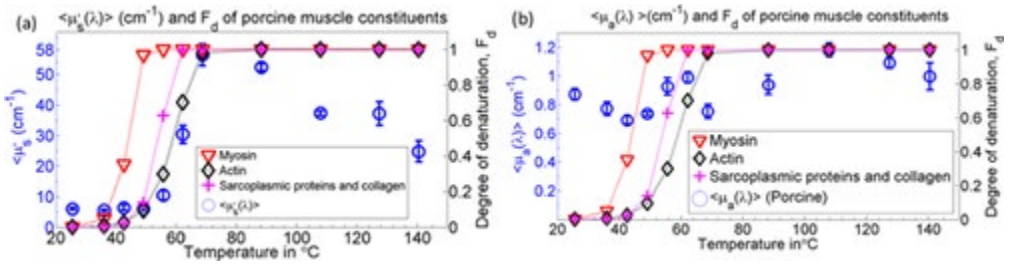

Figure 6 Comparison of changes in (**a**) $<\mu_s'(\lambda)>$ and (**b**) $<\mu_a(\lambda)>$ (right) to F_{d} of myosin, actin, sarcoplasmic proteins, and collagen of porcine tissue at different temperatures. An $F_{\mathrm{d}}\ =\ 1$ denotes complete coagulation.

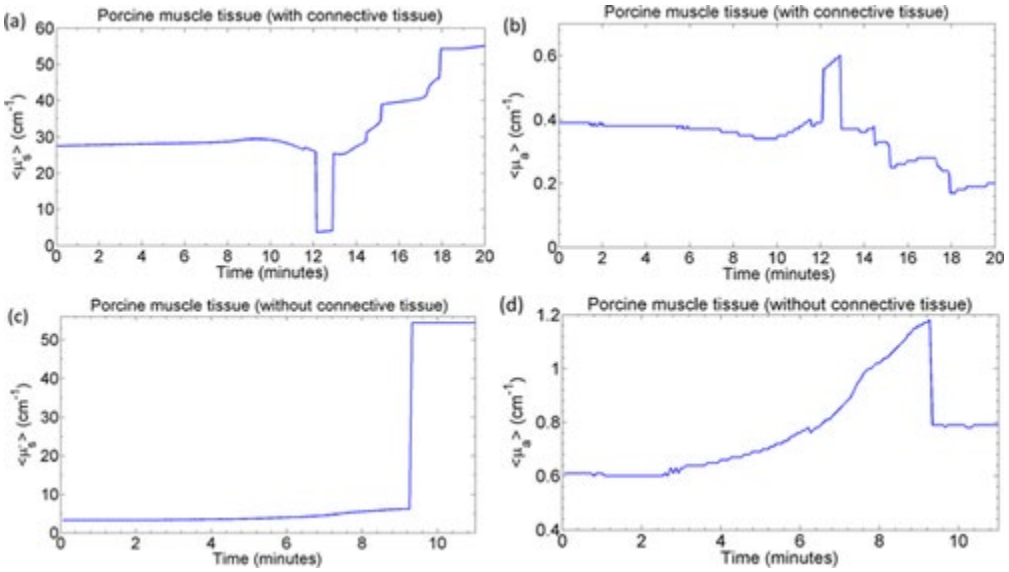

Figure 7 Real-time changes in (**a** and **c**) $<\mu_s'(\lambda)>$ and (**b** and **d**) $<\mu_a(\lambda)>$ during heating of a porcine muscle to a set temperature of 70°C using the set-up in Fig. 2b.

The corresponding temperature where $<\mu_s'(\lambda)>$ plateaued during continuous monitoring of porcine tissues (with connective tissue) was $63.6\ \pm\ 0.7$°C. The $<\mu_s'(\lambda)>$ plateauing observed in the first *ex vivo* experiment Figures **4** and **5** also occurred around similar temperatures ($68.7\ \pm\ 1.7$°C and $57.1\ \pm\ 1.5$°C, respectively). The discrepancy in the plateauing temperatures may have been due to factors such as differences in initial tissue temperatures, tissue thickness, ambient temperature, and thermal tissue parameters such as water content, thermal conductivity *et cetera*. However, the plateauing temperature of porcine tissue (without connective tissue) during continuous monitoring was about 14.7° lower. Further, the decrease in $<\mu_a(\lambda)>$ of coagulating pork tissue samples in Figure **7**d is not clear, but likely due to the heat-induced changes to the absorption spectra of the tissue chromophores. No carbon deposits were observed at the site of measurement during continuous monitoring as the samples were not subjected temperatures above 80°C. If the plateauing of $<\mu_s'(\lambda)>$ did imply complete tissue coagulation, then, we could conclude that our device can detect the point of complete coagulation which could help in minimizing the risk of over/under-ablation during thermal ablation

procedures. However, more studies, particularly with histological diagnosis of the degree of tissue damage, maybe required to understand the relationship between $< \mu_s'(\lambda) >$, and thermal tissue damage.

The change in tissue microstructure and physiology during heating alters the propagation of light within the tissue. These alterations are manifested through changes in the tissue $\mu_a(\lambda)$ and $\mu_s'(\lambda)$. Some of the major light scatterers within biological tissues are mitochondria, cell nuclei, cell membranes etc. Tissue scattering is affected by the refractive index mismatch at membrane boundaries, which changes during heating due to rupturing of cell membranes, coagulation of structural proteins, loss of extracellular fluids or formation of new particles, and so on [54, 55]. The changes in absorption could be due to denaturation of chromophores and tissue shrinkage. However, it is unclear to us at this point to comment on the changes in $< \mu_a(\lambda) >$ during heating. More studies maybe necessary to understand the temperature-dependent absorption of major tissue chromophores.

One of the major limitations of our study is that some of the extracted tissue optical properties fell outside of the range of the probe calibration. Making it difficult to ascertain the error associated with extracting the optical properties beyond the calibration ranges. However, the extracted optical properties outside of the calibration range did not vary much across different samples, implying that the data outside of the calibration might have a more systematic than random errors. It is also necessary to study the relationship between the microscopic changes within the tissue, and the resulting optical properties in both the native and coagulated tissues. Finally, studying the real-time changes in optical properties of more tissue types may be useful as well before moving to *in vivo* studies.

In conclusion, we have demonstrated that tissue absorption and scattering properties can be measured in real-time during thermal ablation of *ex vivo* tissues. This technique could potentially be used to assess the status of tissues in real-time during thermal ablation of solid tumors. Real-time feedbacks about changes in the tissue optical properties allow a radiologist to adjust the thermal dosage during a thermal ablation procedure to achieve an optimal outcome. The DRS system with a side-firing probe reported in this study may provide a low-cost, and portable alternative of MRT and MRI in tumor therapy.

ACKNOWLEDGMENTS

We would like to thank the National institute of Health (NIH) and The University of Akron for their financial support during this research.

References

1 W Busch, Uber den Einfluss welchen Heftigerc Erysipeln Zuweilen auf Organisierte Neubildungen Ausuberi. Verhandl Natiirli Pretrss Rheiri Westplral 1866; **23**: 28– 30.

2 Cavaliere R, Ciocatto EC, Giovanella BC, Heidelberger C, Johnson RO, Margottini M, Mondovi B, Moricca G, Rossi-Fanelli A. Selective heat sensitivity of cancer cells. Biochemical and clinical studies. *Cancer* 1967; **20**: 1351– 1381.

3 Vogl TJ, Farshid P, Naguib NNN, Zangos S. Thermal ablation therapies in patients with breast cancer liver metastases: A review. *Eur Radiol* 2013; **23**: 797– 804.

4 Keane MG, Bramis K, Pereira SP, Fusai GK. Systematic review of novel ablative methods in locally advanced pancreatic cancer. *World J Gastroenterol* 2014; **20**: 2267– 2278.
5 Gharib H, Hegedus L, Pacella CM, Baek JH, Papini E. Clinical review: Nonsurgical, image-guided, minimally invasive therapy for thyroid nodules. *J Clin Endocrinol Metab* 2013; **98**: 3949– 3957.
6 Feng B, Liang P. Local thermal ablation of renal cell carcinoma. *Eur J Radiol* 2012; **81**: 437– 440.
7 Liang P, Wang Y, Yu XL, Dong BW. Malignant liver tumors: Treatment with percutaneous microwave ablation-complications among cohort of 1136 patients. *Radiology* 2009; **251**: 933– 940.
8 Norred SE, Johnson JA. Magnetic resonance-guided laser induced thermal therapy for glioblastoma multiforme: A review. *Biomed Res Int* 2014; **2014**: 761312.
9 Sommer G, Bouley D, Gill H, Daniel B, Pauly KB, Diederich C. Focal ablation of prostate cancer: Four roles for magnetic resonance imaging guidance. *Can J Urol* 2013; **20**: 6672– 6681.
10 Wagstaff P, Ingels A, Zondervan P, de la Rosette JJ, Laguna MP. Thermal ablation in renal cell carcinoma management: A comprehensive review. *Curr Opin Urol* 2014; **24**: 474– 482.
11 Thomasse SC, Denniso AR, Garcea G. Ablation for recurrent hepatocellular carcinoma: A systematic review of clinical efficacy and prognostic factors. *World J Surg* 2015; **39**: 1150– 1160.
12 Chu KF, Dupuy DE. Thermal ablation of tumours: Biological mechanisms and advances in therapy. *Nat Rev Cancer* 2014; **14**: 199– 208.
13 Sturesson C. Interstitial laser-induced thermotherapy: Influence of carbonization on lesion size. *Lasers Surg Med* 1998; **22**: 51– 7.
14 Janda P, Sroka R, Mundweil B, Betz CS, Baumgartner R, Leunig A. Comparison of thermal tissue effects induced by contact application of fiber guided laser systems. *Lasers Surg Med* 2003; **33**: 93– 101.
15 Varghese T, Zagzebski JA, Chen Q, Techavipoo U, Frank G, Johnson C, Wright A, Lee FT. Ultrasound monitoring of temperature change during radiofrequency ablation: Preliminary in vivo results. *Ultrasound Med Biol* 2002; **28**: 321– 329.
16 Arrhenius S. Über die reaktionsgeschwindigkeit bei der inversion von rohrzucker durch Säuren. *Zeitschrift für physikalische Chemie* 1889; **4**: 226– 248.
17 Carpentier A, Chauvet D, Reina V, Beccaria K, Leclerq D, McNichols RJ, Gowda A, Cornu P, Delattre JY. MR-guided laser-induced thermal therapy (LITT) for recurrent glioblastomas. *Lasers Surg Med* 2012; **44**: 361– 368.
18 Rieke V, Butts Pauly K. MR thermometry. *J Magn Reson Imaging* 2008; **27**: 376– 390.
19 Mertyna P, Goldberg W, Yang W, Goldberg SN. Thermal ablation a comparison of thermal dose required for radiofrequency-, microwave-, and laser-induced coagulation in an ex vivo bovine liver model. *Acad Radiol* 2009; **16**: 1539– 1548.
20 Livraghi T, Solbiati L, Meloni F, Ierace T, Goldberg SN, Gazelle GS. Percutaneous radiofrequency ablation of liver metastases in potential candidates for resection the—"Test-of-time" approach. *Cancer* 2003; **97**: 3027– 3035.
21 Ahmed M, Goldberg SN. Thermal ablation therapy for hepatocellular carcinoma. *J Vasc Interv Radiol* 2002; **13**: S231– S244.
22 Jenne JW, Preusser T, Gunther M. High-intensity focused ultrasound: Principles, therapy guidance, simulations, and applications. *Z Med Phys* 2012; **22**: 311– 322.
23 Rosenberg C, Hoffmann COM, Mensel B, Puls R, Hosten N. Laser ablation. *Radiologe* 2012; **52**: 15– 21.
24 Yu B, Shah A, Nagarajan VK, Ferris DG. Diffuse reflectance spectroscopy of epithelial tissue with a smart fiber-optic probe. *Biomed Opt Express* 2014; **5**: 675– 689.
25 Yu B, Nagarajan VK, Ferris DG. Mobile fiber-optic sensor for detection of oral and cervical cancer in the developing world. *Methods Mol Biol* 2015; **1256**: 155– 170.
26 Yu B, Lo JY, Kuech TF, Palmer GM, Bender JE, Ramanujam N. Cost-effective diffuse reflectance spectroscopy device for quantifying tissue absorption and scattering in vivo. *J Biomed Opt* 2008; **13**: 060505.

27 Hafeez U, Atif M, Firdous S, Mehmood MS, Hamza MY, Imran M, Hussain G, Ikram M. Optical properties of normal and thermally coagulated chicken liver tissue measured ex vivo with diffuse reflectance. *Opt Spectros* 2011; **110**: 313– 319.
28 Dressler C, Schwandt D, Beuthan J, Mildaziene V, Zabarylo U, Minet O. Thermally induced changes of optical and vital parameters in human cancer cells. *Laser Phys Lett* 2010; **7**: 817– 823.
29 Wei HJ, Xing D, He BH, Wu RH, Gu HM, Wu GY, Chen XM. Thermal coagulation of human benign prostatic hyperplasia tissues induced changes in the absorption and scattering properties in spectral range from 590 to 1,064 nm in vitro. *Guang Pu Xue Yu Guang Pu Fen Xi* 2008; **28**: 394– 398.
30 Ao H, Xing D, Wei H, Gu H, Wu G, Lu J. Thermal coagulation-induced changes of the optical properties of normal and adenomatous human colon tissues in vitro in the spectral range 400–1,100 nm. *Phys Med Biol* 2008; **53**: 2197– 2206.
31 Holmer C, Lehmann KS, Risk J, Roggan A, Germer CT, Reissfelder C, Isbert C, Buhr HJ, Ritz JP. Colorectal tumors and hepatic metastases differ in their optical properties-relevance for dosimetry in laser-induced interstitial thermotherapy. *Lasers Surg Med* 2006; **38**: 296– 304.
32 Terenji A, Willmann S, Osterholz J, Hering P, Schwarzmaier HJ. Measurement of the coagulation dynamics of bovine liver using the modified microscopic Beer-Lambert law. *Lasers Surg Med* 2005; **36**: 365– 370.
33 Swartling J, Palsson S, Platonov P, Olsson SB, Andersson-Engels S. Changes in tissue optical properties due to radio-frequency ablation of myocardium. *Med Biol Eng Comput* 2003; **41**: 403– 409.
34 Yaroslavsky AN, Schulze PC, Yaroslavsky IV, Schober R, Ulrich F, Schwarzmaier HJ. Optical properties of selected native and coagulated human brain tissues in vitro in the visible and near infrared spectral range. *Phys Med Biol* 2002; **47**: 2059– 2073.
35 Parekh DJ, Chiang LW, Herrell SD. In vivo assessment of radio frequency induced thermal damage of kidney using optical spectroscopy. *J Urol* 2006; **176**: 1626– 1630.
36 Buttemere CR, Chari RS, Anderson CD, Washington MK, Mahadevan-Jansen A, Lin WC. In vivo assessment of thermal damage in the liver using optical spectroscopy. *J Biomed Opt* 2004; **9**: 1018– 1027.
37 Anderson CD, Lin WC, Buttemere CR, Washington MK, Mahadevan-Jansen A, Pierce J, Nicoud IB, Pinson CW, Chari RS. Real-time spectroscopic assessment of thermal damage: Implications for radiofrequency ablation. *J Gastrointest Surg* 2004; **8**: 660– 669.
38 Lin WC, Buttemere C, Mahadevan-Jansen A. Effect of thermal damage on the in vitro optical and fluorescence characteristics of liver tissue's. *IEEE J* 2003; **9**: 162– 170.
39 Ramanujam N. Fluorescence spectroscopy of neoplastic and non-neoplastic tissues. *Neoplasia* 2000; **2**: 89– 117.
40 JD Johansson, A Zerbinati, K Wardell, Diffuse reflectance spectroscopy during experimental radio frequency ablation. 14th nordic-baltic conference on biomedical engineering and medical physics **20** 2008; 371– 374.
41 Yoshimura H, Viator JA, Jacques SL. Relationship between damaged fraction and reflected spectra of denaturing tissues. *Lasers Surg Med* 2005; **37**: 308– 313.
42 Hsu CP, Razavi MK, So SK, Parachikov IH, Benaron DA. Liver tumor gross margin identification and ablation monitoring during liver radiofrequency treatment. *J Vasc Interv Radiol* 2005; **16**: 1473– 1478.
43 Anderson CD, Lin WC, Beckham J, Mahadevan-Jansen A, Buttemere CR, Pierce J, Nicoud IB, Pinson CW, Chari RS. Fluorescence spectroscopy accurately detects irreversible cell damage during hepatic radiofrequency ablation. *Surgery* 2004; **136**: 524– 531.
44 Tanis E, Spliethoff JW, Evers DJ, Langhout GC, Snaebjornsson P, Prevoo W, Hendriks BH, Ruers TJ. Real-time in vivo assessment of radiofrequency ablation of human colorectal liver metastases using diffuse reflectance spectroscopy. *Ejso* 2016; **42**: 251– 259.
45 Adams MT, Wang Q, Cleveland RO, Roy RA. Thermal dose dependent optical property changes of ex vivo chicken breast tissues between 500 and 1100 nm. *Phys Med Biol* 2014; **59**: 3249– 3260.

46 Yu B, Shah A, Wang B, Rajaram N, Wang Q, Ramanujam N, Palmer GM, Dewhirst MW. Measuring tumor cycling hypoxia and angiogenesis using a side-firing fiber optic probe. *J Biophotonics* 2014; **7**: 552– 564.
47 Patterson MS, Andersson-Engels S, Wilson BC, Osei EK. Absorption spectroscopy in tissue-simulating materials: A theoretical and experimental study of photon paths. *Appl Opt* 1995; **34**: 22– 30.
48 Palmer GM, Ramanujam N. Monte Carlo-based inverse model for calculating tissue optical properties. Part I: Theory and validation on synthetic phantoms. *Appl Opt* 2007; **46**: 6847.
49 Shino Kajitani MF, Sakai Noboru. Kinetics of thermal denaturation of protein in cured pork meat. *Japan J Food Eng* 2011; **12**: 19– 26.
50 Alali S, Ahmad M, Kim A, Vurgun N, Wood MFG, Vitkin IA. Quantitative correlation between light depolarization and transport albedo of various porcine tissues. *J Biomed Opt* 2012; **17**(4): 0450041– 0450048.
51 Cheong W-F, Prahl SA, Welch AJ. A review of the optical properties of biological tissues. *IEEE J Quantum Electron* 1990; **26**: 2166– 2185.
52 Kienle A, Lilge L, Patterson MS, Hibst R, Steiner R, Wilson BC. Spatially resolved absolute diffuse reflectance measurements for noninvasive determination of the optical scattering and absorption coefficients of biological tissue. *Appl Opt* 1996; **35**: 2304– 2314.
53 Ao HL, Xing D, Wei HJ, Gu HM, Wu GY, Lu JJ. Thermal coagulation-induced changes of the optical properties of normal and adenomatous human colon tissues in vitro in the spectral range 400–1100 nm. *Phys Med Biol* 2008; **53**: 2197– 2206.
54 Thomsen S, Jacques S, Flock S. Microscopic correlates of macroscopic optical property changes during thermal coagulation of myocardium. *Proc Laser-Tissue Interaction* 1990; **1202**: 2– 11.
55 Thomsen S. Pathological analysis of photothermal and photomechanical effects of laser-tissue interactions. *Photochem Photobiol* 1991; **53**: 825– 835.